

**COMPARING MODELS OF RAPIDLY ROTATING
RELATIVISTIC STARS CONSTRUCTED BY TWO
NUMERICAL METHODS**

Nikolaos Stergioulas and John L. Friedman

Department of Physics, University of Wisconsin-Milwaukee, PO Box 413, Milwaukee, WI
53201

email: niksterg@alpha2.csd.uwm.edu, friedman@thales.phys.uwm.edu

Received _____; accepted _____

ABSTRACT

We present the first direct comparison of codes based on two different numerical methods for constructing rapidly rotating relativistic stars. A code based on the Komatsu-Eriguchi-Hachisu (KEH) method (Komatsu *et al.* 1989), written by Stergioulas, is compared to the Butterworth-Ipser code (BI), as modified by Friedman, Ipser and Parker. We compare models obtained by each method and evaluate the accuracy and efficiency of the two codes. The agreement is surprisingly good, and error bars in the published numbers for maximum frequencies based on BI are dominated not by the code inaccuracy but by the number of models used to approximate a continuous sequence of stars. The BI code is faster per iteration, and it converges more rapidly at low density, while KEH converges more rapidly at high density; KEH also converges in regions where BI does not, allowing one to compute some models unstable against collapse that are inaccessible to the BI code. A relatively large discrepancy recently reported (Eriguchi *et al.* 1994) for models based on the Friedman-Pandharipande equation of state is found to arise from the use of two different versions of the equation of state. For three representative equations of state, the 2-dimensional space of equilibrium configurations is displayed as a surface in a 3-dimensional space of angular momentum, mass, and central density. We find, for a given equation of state, that equilibrium models with maximum values of mass, baryon mass, and angular momentum are (generically) either all unstable to collapse or are all stable. In the first case, the *stable* model with maximum angular velocity is also the model with maximum mass, baryon mass, and angular momentum. In the second case, the stable models with maximum values of these quantities are all distinct. Our implementation of the KEH method will be available as a public domain program for interested users.

Subject headings: stars: neutron — stars: rotation

PACS: 4.40.Dg, 95.30.Sf, 97.10.Kc, 97.60.Jd

1. Introduction

Models of rapidly rotating relativistic stars have been constructed by a number of different groups, using a few somewhat different numerical methods (see Friedman (1994) for a bibliography). Recent work has been based on the BI code (Friedman et al. 1986 (FIP), 1989; Lattimer et al. 1990), on the KEH code (Komatsu et al. 1989a, 1989b; Cook et al. 1992, 1994a, 1994b; Eriguchi et al. 1994; Nishida et al. 1992, 1994; Hashimoto et al. 1994), and on a code using a finite element method (Neugebauer & Herlt 1984; Wu et al. 1991; Neugebauer & Herold 1992). No group has used more than one code, and, as we will see, discrepancies in reported results reflect differences in versions of the same equation of state (EOS) and in the number of stellar models used to compute sequences, as well as numerical error intrinsic to the codes.¹

The present paper reports a direct comparison of models of rotating neutron stars constructed with two different codes. Models are computed using the FIP implementation of the BI method, and corresponding models are constructed using a code written independently by Stergioulas, based on the Cook et al. implementation of the KEH method. We find good agreement between corresponding models. Sensitive quantities, such as the radius and quantities that depend on it, agree to better than 2%, despite the fact that the BI code used only 6 spokes (for one quadrant) and 60 radial grid points, because of limited computer speed at the time it was implemented. We used three EOSs, G (excessively soft), C, and L (excessively stiff), to span a range of compressibility larger than that allowed by current knowledge of neutron-star matter. Models based on two other EOSs, FP and A, were also computed to compare them with results given in Eriguchi et al. (1994).

Our implementation of the KEH method is used to construct the two-dimensional family of equilibrium models for EOSs C, L and FP. The surface of equilibria is ruled by sequences of constant baryon mass and angular momentum, from which one obtains the boundary of the region of configurations stable to axisymmetric perturbations.

Our KEH code has been automated to construct various sequences of neutron star models and will be available as a public domain program.

2. Outline of the numerical methods.

¹After this paper was written, we received a copy of a preprint by Salgado et. al. (1994) reporting results from a new code based on a method different from those listed here.

The BI and KEH methods are described in detail in Butterworth & Ipser (1976) and in Komatsu et al. (1989a) and Cook et al. (1992), but an outline of their similarities and differences may be helpful (for a review of stellar structure prior to 1992, see Friedman & Ipser 1993). Following Bardeen & Wagoner (1971), both methods use the same chart, describing the geometry of an axisymmetric rotating star by a metric of the form $ds^2 = -e^{2\nu} dt^2 + e^{2\psi}(d\phi - \omega dt)^2 + e^{2\mu}(dr^2 + r^2 d\theta^2)$, with Killing vectors ∂_t and ∂_ϕ (potentials independent of ϕ and t). Each method solves, equation-by-equation, the same set of four field equations and the integrated equation of hydrostatic equilibrium.

Although the gauge and the set of equations used are identical, the iterative procedure differs in two ways. To go from the k th to the $(k+1)$ st approximation to a star, both methods solve one equation at a time for one potential at a time. In BI this is done to reduce the matrix one inverts to a manageable size. (With present computers, handling one potential at a time is less essential, but it may still be the most efficient method). KEH is designed for a one-potential approach and does not seem to allow a variant in which one solves simultaneously for the set of perturbed potentials. The BI iteration differs from a Newton-Raphson iteration only in this truncation. KEH observe that one can write the exact second-derivative terms as flat-space derivative operators acting on redefined potentials. This allows them to invert the (truncated) linearized operators by using explicit flat-space Green functions. One can view their iteration as departing from Newton-Raphson by omitting the linearized part of the operator that is not flat. This relation between the KEH method and Newton Raphson can be seen as follows: First, for simplicity, consider a single nonlinear equation for a single field ϕ ,

$$L\phi = S(\phi), \tag{1}$$

where L is a linear operator, and S is nonlinear. Given ϕ_k , one obtains $\phi_{k+1} = \phi_k + \delta\phi$ via Newton-Raphson by writing

$$L\delta\phi - S'(\phi_k)\delta\phi = -L\phi_k + S(\phi_k).$$

This is identical to solving

$$L\phi_{k+1} - S'(\phi_k)\delta\phi = S(\phi_k).$$

In the KEH method, one solves the equation,

$$L\phi_{k+1} = S(\phi_k), \tag{2}$$

which can be regarded as the result of replacing the linearized operator $L - S'(\phi_k)$ occurring in the Newton-Raphson scheme by the truncated version L .²

²Our discussion clarifies the relation between KEH and Newton-Raphson; but the KEH

For each of the three metric potentials that satisfy an elliptic equation, the KEH iteration conforms to the above description. In particular, consider Eq. (4) of KEH, for the potential $f \equiv \rho e^{\gamma/2}$. If one were to follow BI, one would obtain the $(k+1)$ st value of the potential from the k th value of f and from the set Q_k of other potentials by solving

$$\nabla^2 \delta f - \frac{\delta S_\rho}{\delta f}(f_k, Q_k) \delta f = -\nabla^2 f_k + S_\rho(f_k, Q_k),$$

to find

$$f_{k+1} = f_k + \delta f.$$

If one omits the term $\frac{\delta S_\rho}{\delta f}(f_k, Q_k)$, the resulting equation

$$\nabla^2 \delta f = -\nabla^2 f_k + S_\rho(f_k, Q_k),$$

is identical to KEH,

$$\nabla^2 f_{k+1} = S_\rho(f_k, Q_k).$$

The other elliptic equations for the potentials are handled by KEH in essentially the same way.

The second key difference in the methods is in the quantities held fixed at each iteration: BI fix the polar redshift and angular velocity, while KEH fix the ratio r_p/r_e of values of the coordinate r at the pole and equator and the central density.

In our implementation of KEH, the first order derivatives are approximated by a standard three-point formula. For the second derivative, however, we found that, if one uses a standard three-point formula (as in Eriguchi et al. 1994) the metric potential μ oscillates in most of the interior of the star along a radial spoke. We overcame the problem by using twice the grid spacing to evaluate the second derivatives, which resulted in all metric potentials being smooth functions of radius and angle. If one does not follow the above procedure to assure the smoothness of the potentials, the errors introduced in the physical quantities can range from $\sim 0.5\%$ in the mass, and radius to $\sim 2\%$ in other quantities, such as the angular velocity, angular momentum, and redshifts for maximum mass models.

3. Internal checks and the nonrotating limit of the KEH code

iteration converges to a solution not because of that relation, but because Eq. (2) is an example of the method of successive substitution (see, e.g., Nakamura 1993). That is, when ϕ_k given by (2) converges, it converges to an exact solution, because Eq. (1) is exact.

The accuracy of the physical quantities in a computed model depends on the grid-size and the domain of integration. BI and Eriguchi et al. (1994) integrate over a spherical region of radius equal to about twice the equatorial radius of the star. We integrate over all space using the coordinate transformation introduced by Cook et al. (1994). The size of the grid that we use is 129×65 (radial \times angular), which is similar to the one used by Cook et al. (1994) and Eriguchi et al. (1994). Doubling the grid-points in both directions did not change any physical quantity by more than 0.1 %.

Our code was checked in the nonrotating limit, by constructing sequences of spherical models and comparing them to models published in Arnett & Bowers (1977). Along a sequence of nonrotating models, the maximum differences between the two codes in the mass and radius are $\lesssim 0.3\%$ and become consistently smaller as one increases the number of grid points.

4. Comparison of rotating neutron star models.

The two codes were first compared for slowly rotating models. A typical model is shown in Table 1. The agreement in the mass and angular velocity is $\sim 0.2\%$ while the metric potentials agree to within 0.01% to 0.4%. The two radii differ by 1.4%. Next, we compare rapidly rotating models, which are near the maximum mass (reported as the maximum mass models in FIP), for EOS C, L, and G (Table 1). Here the agreement ranged from 0.1% to 0.6% for the masses and from 0.3% to 1.2% for the radii. The angular velocities agreed to $\sim 0.2\%$ and most other quantities to $\lesssim 0.5\%$, except for some quantities for EOS G and L which differed by a few per cent. Fig. 1 compares results of the BI and KEH codes for the metric potential ω as a function of coordinate radius in the equatorial plane for the two rapidly rotating, EOS C models in Table 1. The two curves almost coincide, and the agreement in the other three metric potentials for the above two models was slightly better. FIP estimate the accuracy of their results to be $\sim 1\%$ in the mass, metric coefficients, density and pressure distributions while the accuracy of the radius and quantities that depend on it is estimated at $\sim 5\%$. The differences in the above comparisons were somewhat better than this, implying an accuracy in finding the location of the surface that is somewhat (but not dramatically) better than the grid spacing. The vast increase in computer speed since the BI code was written allows a much finer grid and correspondingly greater accuracy in surface finding.

To compare the convergence for the two codes, we used as input for each code a fixed initial model and required the code to converge to the same final model, for which the

initial model served as an inaccurate guess. The number of iterations required increases considerably for both codes as one approaches the maximum mass. BI exploits the fact that stellar structure is dominated by the lowest-order multipoles $P_l(\cos\theta)$, and uses a grid of size 60×6 , with 6 radial spokes in a quadrant. This means one truncates the multipole expansion above $l = 12$. Fig. 2 compares the number of iterations needed to obtain a given accuracy in $|\delta g^{tt}/g^{tt}|$ for a rapidly rotating, high density model. For the same accuracy, KEH needs a larger grid and a longer time per iteration: On the DEC Alpha we used, BI required 0.2 s/iteration, compared to 0.7 s/iteration for KEH, for grids yielding comparable error. Because roughly the same number of iterations were required for the same accuracy for low-density models, BI was more than three times as fast, but KEH came into its own for the highest density models, near and above maximum mass. KEH requires fewer iterations near the maximum mass model, and it has additional advantages: (i) except for the lowest density models, BI typically requires one to multiply the inhomogeneous terms by a parameter $c < 1$ to obtain a convergent iteration, and time is spent adjusting c as central density or angular velocity increase along a sequence (KEH did not require any such parameter in order to converge, except for very high density, unstable models constructed with EOS FP). (ii) Although BI successfully computes the full range of equilibria for realistic EOSs, KEH is more robust, allowing one to compute a wider range of models unstable to collapse. (iii) The code can be easily written to allow the user to specify the grid size.

We compared models computed with the KEH code to corresponding models in Cook et al. (1994) and in Eriguchi et al. (1994) and found them in good agreement (maximum 1-2 % differences in physical quantities).³ Eriguchi et al. (1994) compared their results to Friedman et al. (1989) and found similarly good agreement except for EOS FP (Friedman & Pandharipande 1981). For this EOS, the two Ω_K vs. M curves substantially disagreed (where Ω_K is the angular velocity at the mass-shed limit); there was a 5 % discrepancy in the maximum angular velocity and a larger (25 %) difference in the central densities of the maximum-mass configurations. This seemed worrisome, but the difference between the computed models turns out to be almost entirely due to a difference in the version of the EOS used. Using our KEH code, we recomputed the Ω_K vs. M curve for EOS FP, and found it to be close to the corresponding curve in Friedman et al. (1989), (Fig. 3). A computation of the same curve using the version communicated to us by Eriguchi of the FP EOS gave a curve that is similarly close to that of Eriguchi et al (1994). For the version of FP used in FIP, models with the same central density based on the KEH and BI codes

³This agreement is equivalent to that just reported by Salgado et al. (1994) with whom our KEH code also agrees to within 1-2%.

agree in all quantities to within 3% (which includes the error in determining Ω_K). There is a larger difference in the value of ϵ_c at the maximum mass model, because the error in Ω_K is multiplied by a large value of $\partial\epsilon_c/\partial\Omega_K$ (where the derivative is evaluated along a sequence of models at the mass-shed limit).

The frequency Ω_s of a satellite in circular orbit at the star’s equator decreases monotonically as Ω (and hence the radius of the star) increases, with $|d\Omega_s/d\Omega|_{\epsilon_c}$ and $|d\Omega_s/d\Omega|_{M_0}$ apparently diverging at $\Omega = \Omega_s \equiv \Omega_K$ (Fig. 4). One can exploit the steep slope to accurately determine Ω_K . Because the apparent divergence in $|d\Omega_s/d\Omega|$ arises from a similar divergence in $|dR/d\Omega|$ (Fig. 5) one needs that high accuracy to determine R and quantities which depend on it.

5. Surfaces of equilibria

The equilibrium models for a given EOS comprise a 2-dimensional surface. Our KEH code is automated to construct sequences of constant angular momentum and sequences of constant baryon mass, terminating at $\Omega = \Omega_K$. For a given EOS, we first construct the nonrotating sequence and the $\Omega = \Omega_K$ sequence. The code then uses this information to construct a specified number of constant J and constant M_0 (baryon mass) sequences, ruling the 2-dimensional surface of equilibria.

The corresponding surfaces for EOSs C,L and FP are shown in Figs. 6 to 8. These equations of state are substantially different, leading to stars whose maximum values of J differ by more than a factor of two. But their ruled surfaces of equilibria are strikingly similar, and the similarity seen in the figures persists for the other equations of state we have examined. On each surface, the ridge of maximum mass at fixed J (or minimum mass at fixed baryon mass M_0) marks the onset of axisymmetric instability (instability to collapse) (Friedman, Ipser & Sorkin 1988, Cook et al. 1992). Stars stable against collapse lie on the low-density side of the dashed line on each surface. The surfaces fold over at the ridge, and the diagrams display a sharp contrast between an apparent cusp at the maximum mass configuration in the $J - M$ plane and the smooth unprojected boundary of the surface itself.

FIP noted that among all stable models, the model with maximum mass appeared also to have the maximum Ω , J , and M_0 , and this apparent coincidence can be seen in Figs. 6 to 8. As Cook et al. (1992,1994a,b) have found, there is often a slight difference between the models of maximum M and Ω , and a check of their claim for EOSs L and FP is shown

in Figs. 9 and 10, which depict the region very near the maximum mass model. In addition, we found that models with maximum values of J and M_0 can also fail to coincide exactly with the maximum Ω model and this can be seen from the following argument: The models with maximum Ω and maximum M among all equilibria do not coincide. Thus either $\epsilon_c(\Omega_{\max}) < \epsilon_c(M_{\max})$ or $\epsilon_c(\Omega_{\max}) > \epsilon_c(M_{\max})$. In the first case, stable models with maximum M , Ω , J and M_0 coincide. In the second case, $(\partial M/\partial \epsilon_c)_J > 0$ for any $\epsilon_c < \epsilon_c(\Omega_{\max})$, and $J(M_{\max}) > J(\Omega_{\max})$. Furthermore, $\partial M/\partial \epsilon_c = 0$ at the maximum mass model. Hence, there exists $\epsilon_c < \epsilon_c(M_{\max})$ with $J > J(M_{\max})$. A similar argument, using $(\partial M/\partial \epsilon_c)_{M_0}$, yields $\epsilon_c(M_{0\max}) \neq \epsilon_c(M_{\max})$, (see Figs. 9 and 10).

Depending on the central density of the fastest rotating stable model we can distinguish two classes of equations of state: if the fastest rotating stable model is at a lower density than the maximum mass equilibrium model, the *equilibrium* models with maximum M, M_0 , and J are all unstable (e.g. EOS FP, Fig. 10); otherwise they are all stable (e.g. EOS L, Fig. 9). We note that in the first case, the fastest rotating *stable* model is also the configuration with maximum M, M_0 , and J , while in both cases the four different *equilibrium* models are all distinct. Even when the coincidence of stable models is not precise, the models with maximum M , Ω , J and M_0 are generally very close in central density (with the exception of EOS M (see Cook et al. 1994b)). As a result, they *appear* to coincide with the sharp edge in the M - J plots (Figs. 6 to 7).

We thank Y. Eriguchi for useful discussions and for providing us with his version of EOS FP and detailed numerical results for selected models. This research has been supported by NSF grant PHY-9105935.

REFERENCES

- Arnett, W. D., & Bowers, R. L. 1977, *ApJS*, 33, 415
- Bardeen, J. M., & Wagoner, R. V. 1971, *ApJ*, 167, 359
- Bethe, H. A. and Johnson, M. 1974, *Nucl. Phys.*, A230, 1
- Butterworth, E. M., & Ipser, J. R. 1976, *ApJ*, 204, 200
- Cook, G. B., Shapiro, S. L., & Teukolsky, S. A. 1992, *ApJ*, 398, 203
- Cook, G. B., Shapiro, S. L., & Teukolsky, S. A. 1994a, *ApJ*, 422, 227
- Cook, G. B., Shapiro, S. L., & Teukolsky, S. A. 1994b, *ApJ*, 424, 823
- Eriguchi, Y., Hachisu & Nomoto, K. 1994, *MNRAS*, 266, 179
- Friedman, B., & Pandharipande, V. R. 1981, *Nucl. Phys.*, A361, 502
- Friedman, J. L. 1994, *Proceedings of the 1994 Aspen Conference on Millisecond Pulsars*, in press
- Friedman, J. L., & Ipser, J. R. 1993, *Phil. Trans. R. Soc. Lond.*, A340, 391
- Friedman, J. L., Ipser, J. R., & Parker, L. 1986, *ApJ*, 304, 115-139. Erratum, *ApJ*, 351, 705
- Friedman, J. L., Ipser, J. R., & Parker, L. 1989, *Phys. Rev Lett.*, 62, 3015-3019
- Friedman, J. L., Ipser, J. R., & Sorkin, R. D. 1988, *ApJ*, 325, 722
- Hashimoto, M., Oyamatsu, K., & Eriguchi, Y. 1994, preprint
- Komatsu, H., Eriguchi, Y., & Hachisu, 1989*a*, *MNRAS*, 237, 355
- Komatsu, H., Eriguchi, Y., & Hachisu, 1989*b*, *MNRAS*, 239, 153
- Lattimer, L. M., Prakash M., Masak D., & Yahil A., 1990, *ApJ*, 355, 241
- Nakamura, S. 1993, *Applied Numerical Methods in C* (Englewood Cliffs:Prentice Hall)
- Neugebauer, G., & Herlt, E. 1984, *Class. Quant. Grav.*, 1, 695
- Neugebauer, G., & Herold, H. 1992, *Proc. of the Bad Honnef Meeting on Relativity and Gravitational Physics*, ed. Schäfer (Berlin:Springer)
- Nishida, S., Eriguchi, Y., & Lanza, A. 1992, *ApJ* 401, 618
- Nishida, S., Eriguchi, Y., 1994, preprint
- Wu, X., Mütter, H., Soffel, M., Herold, H., & Ruder, H. 1991, *A & A*, 246, 411
- Salgado, M., Bonazzola, S., Gourgoulhon, E., and Haensel, P., *Astron. and Ap.*, in press.

Fig. 1.— Comparison of the metric potential ω at the equatorial plane for the two rapidly rotating, EOS C models shown in Table 1. The horizontal axis shows the coordinate radius r , while the values of Ω and r_e of the model constructed with the KEH code were used to scale the two axes. The two curves almost coincide.

Fig. 2.— The fractional change in g^{tt} is plotted against the number of iterations for a high density, EOS C model. The solid line was obtained with the BI code and the dashed line with the KEH code.

Fig. 3.— Angular velocity vs. mass plot depicting sequences of models at the mass-shed limit for EOSs C, A, and FP. Solid lines are present results, long dashed lines are Eriguchi et al. (1994) results, and short dashed lines are FIP results. FP (E) is the version of the FP EOS that Eriguchi et al. used.

Fig. 4.— The frequency Ω_s of a satellite in circular orbit at the equator drops sharply as the star approaches the mass-shed limit. The above sequence of models was constructed with EOS L and with constant $\epsilon_c = 1.21 \times 10^{15} \text{gr/cm}^3$.

Fig. 5.— The radius R of a star increases sharply as the star approaches the mass-shed limit. The sequence of models is that of Fig. 4.

Fig. 6.— The 2-D surface of equilibrium models is embedded in the J - M - ϵ_c space. The surface is bounded by the spherical ($J = 0$) and Keplerian ($\Omega = \Omega_K$) limits and formed by constant J and constant M_0 sequences (solid lines). Also shown are the axisymmetric instability sequence (short-dashed line), the projections on the J - M plane (long-dashed lines), and the overlapping of the surface in the J - M plane (dotted lines).

Fig. 7.— Surface of equilibrium models for EOS L.

Fig. 8.— Surface of equilibrium models for EOS FP.

Fig. 9.— Detail near M_{max} of the mass vs. central density plot for EOS L. Four different stable models are associated with maximum values of M , M_0 , J , and Ω . Solid lines are constant J sequences, the short-dashed line is the mass-shed limit, and the long-dashed line is the axisymmetric instability sequence. A 257×129 grid was used for high accuracy.

Fig. 10.— Same as Fig. 9, but for EOS FP. A single stable model has maximum values of M , M_0 , J , and Ω .

This figure "fig1-1.png" is available in "png" format from:

<http://arxiv.org/ps/astro-ph/9411032v1>

This figure "fig2-1.png" is available in "png" format from:

<http://arxiv.org/ps/astro-ph/9411032v1>

This figure "fig3-1.png" is available in "png" format from:

<http://arxiv.org/ps/astro-ph/9411032v1>

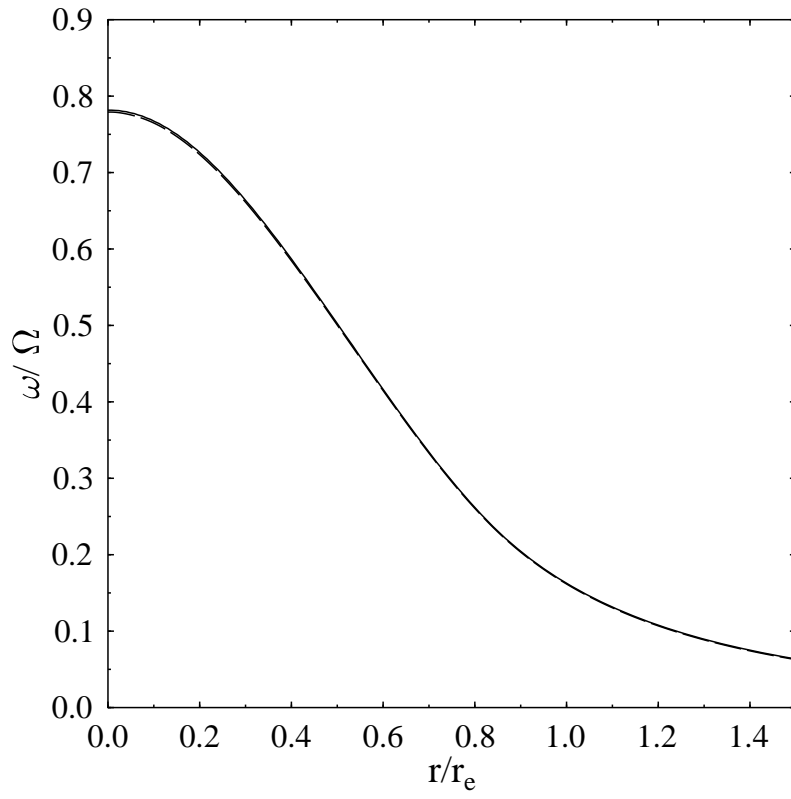


Fig. 1

TABLE 1
COMPARISON OF ROTATING NEUTRON STAR MODELS OBTAINED BY THE TWO CODES.

EOS	Code	ϵ_c (10^{15} gr/cm ³)	M/M_\odot	R (km)	Ω (10^4 s ⁻¹)	cJ/GM_\odot^2	β	T/W	ν_c ^a	B_c ^a	μ_c ^a	ω_c ^a (10^4 s ⁻¹)
C (slow model)	KEH	0.984	1.32	12.1	0.150	2.19	0.676	0.004	-0.424	0.949	0.371	0.639
	BI	0.984	1.32	12.3	0.150	2.17	0.676	0.004	-0.423	0.949	0.371	0.637
C	KEH	2.64	2.17	13.3	1.072	2.99	0.350	0.1091	-1.134	0.752	0.848	0.838
	BI	2.64	2.16	13.2	1.071	2.97	0.352	0.1095	-1.131	0.753	0.847	0.835
G	KEH	5.48	1.55	8.63	1.521	1.45	0.339	0.098	-1.23	0.711	0.891	1.223
	BI	5.48	1.55	8.60	1.524	1.49	0.340	0.101	-1.22	0.718	0.890	1.220
L	KEH	1.10	3.20	17.2	0.762	6.81	0.326	0.122	-1.09	0.769	0.830	0.588
	BI	1.11	3.18	17.3	0.764	6.88	0.340	0.122	-1.07	0.786	0.828	0.582

^aMetric potentials evaluated at the center of the star (B as defined in BI)

This figure "fig1-2.png" is available in "png" format from:

<http://arxiv.org/ps/astro-ph/9411032v1>

This figure "fig2-2.png" is available in "png" format from:

<http://arxiv.org/ps/astro-ph/9411032v1>

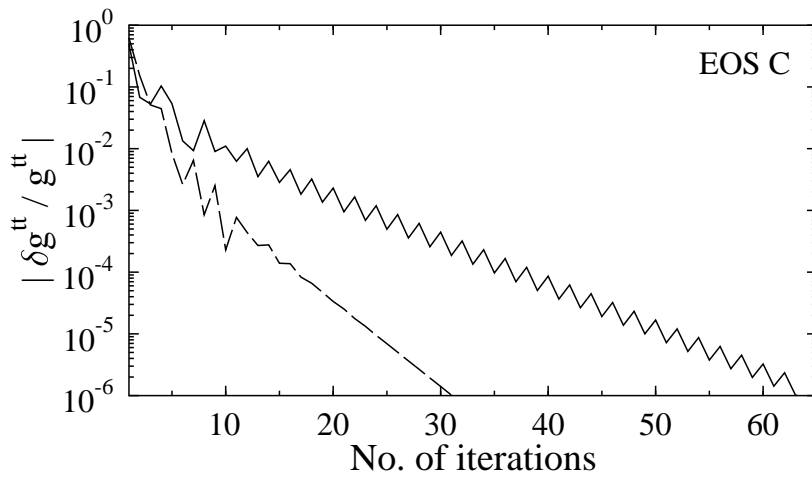


Fig. 2

This figure "fig1-3.png" is available in "png" format from:

<http://arxiv.org/ps/astro-ph/9411032v1>

This figure "fig2-3.png" is available in "png" format from:

<http://arxiv.org/ps/astro-ph/9411032v1>

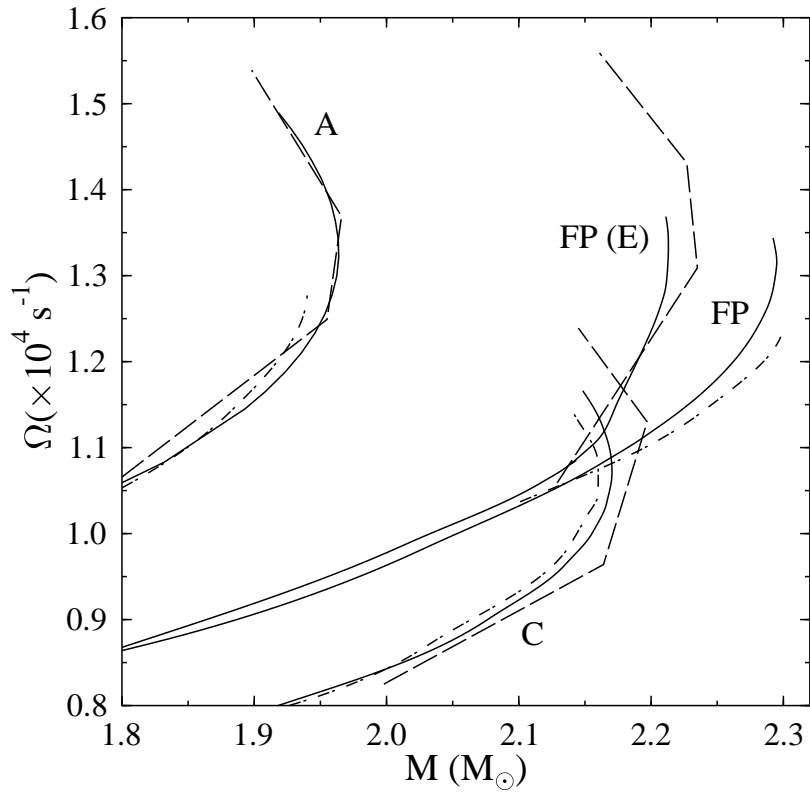


Fig. 3

This figure "fig1-4.png" is available in "png" format from:

<http://arxiv.org/ps/astro-ph/9411032v1>

This figure "fig2-4.png" is available in "png" format from:

<http://arxiv.org/ps/astro-ph/9411032v1>

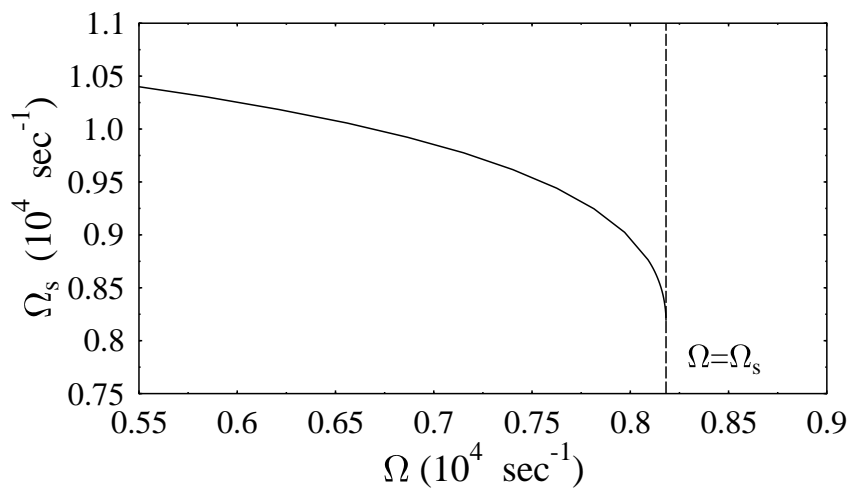


Fig. 4

This figure "fig1-5.png" is available in "png" format from:

<http://arxiv.org/ps/astro-ph/9411032v1>

This figure "fig2-5.png" is available in "png" format from:

<http://arxiv.org/ps/astro-ph/9411032v1>

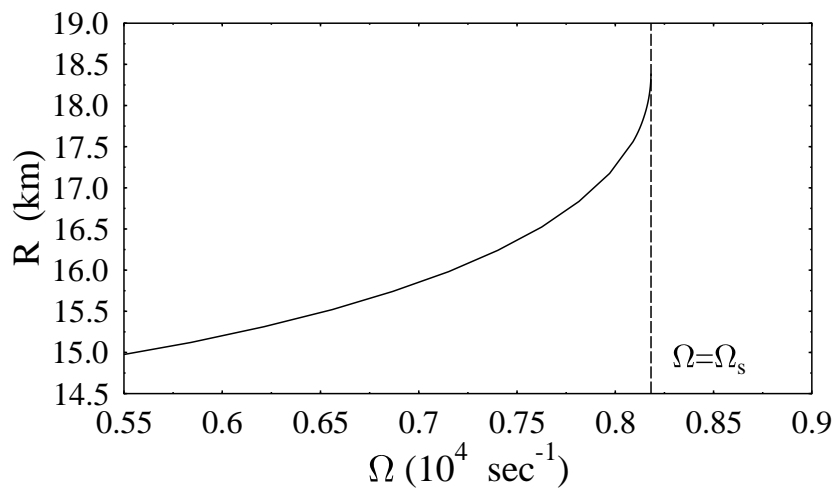


Fig. 5

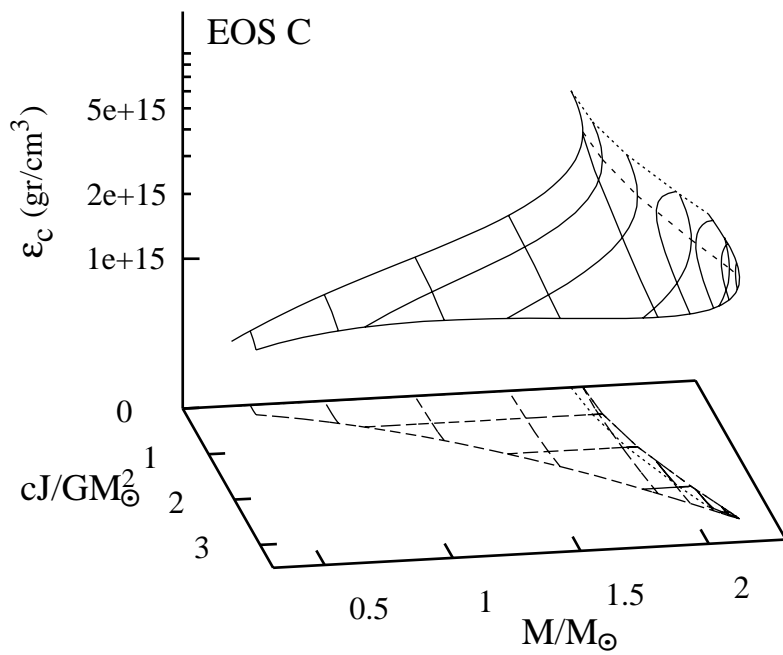


Fig. 6

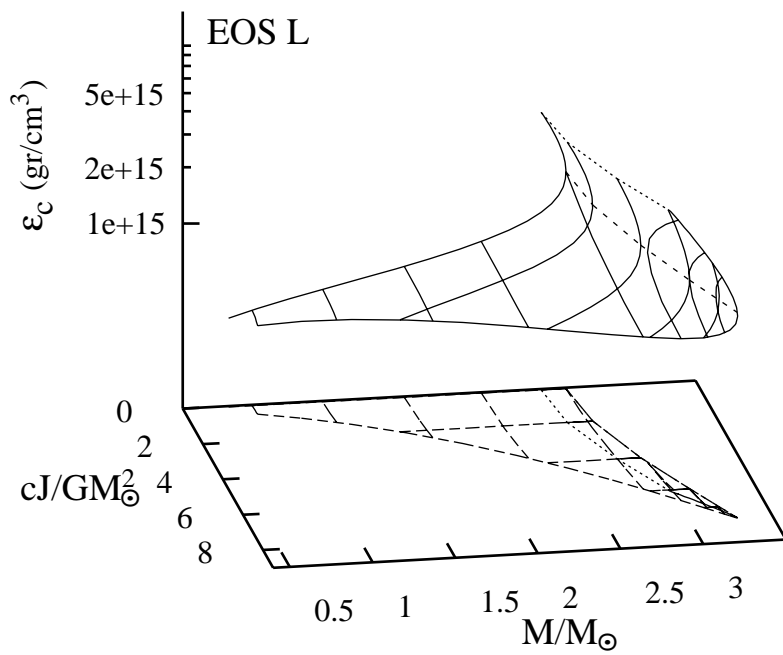


Fig. 7

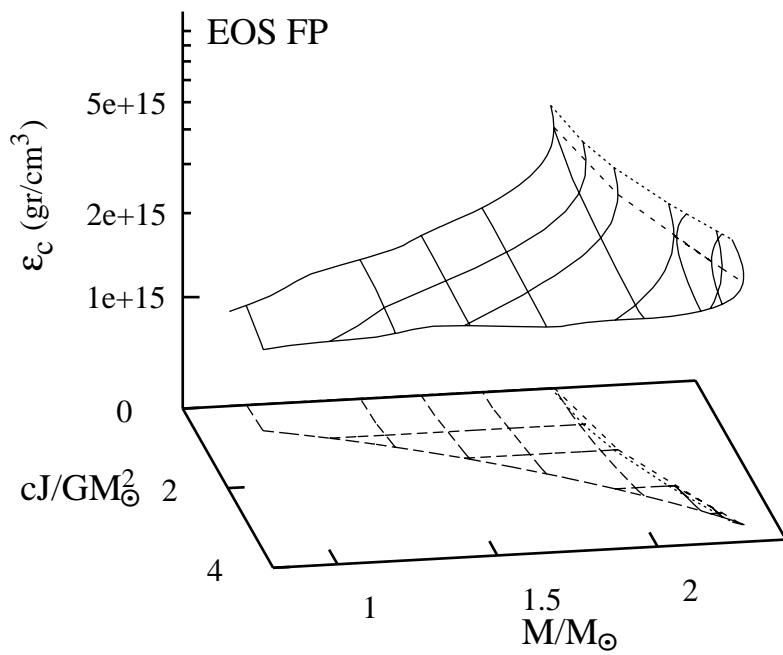


Fig. 8

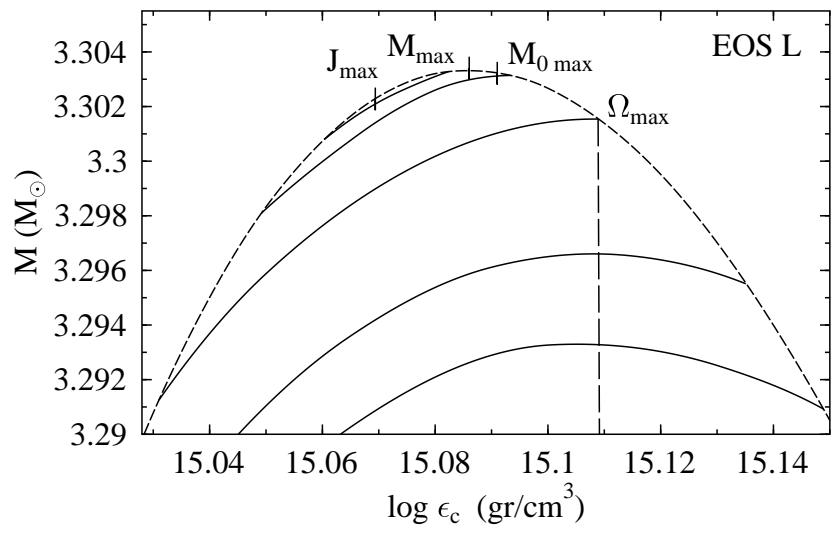


Fig. 9

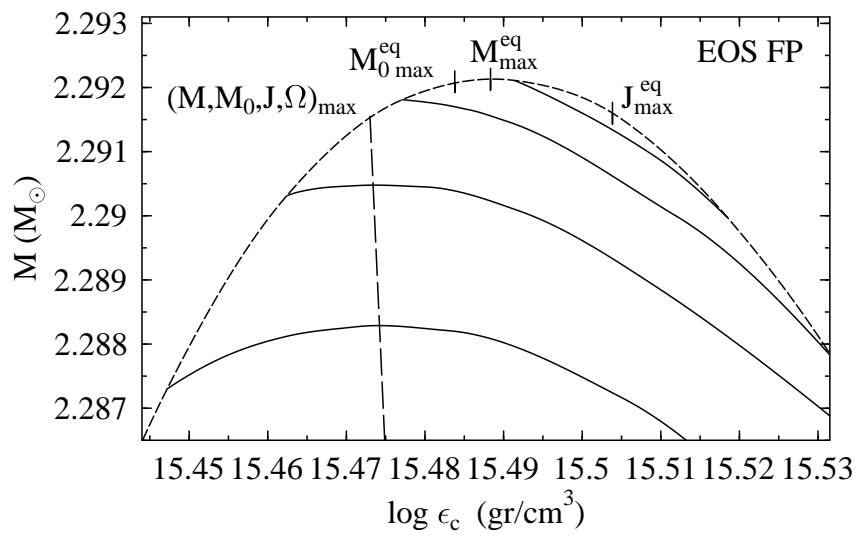


Fig. 10